Giga-seal solvent-free bilayer lipid membranes: from single nanopores to nanopore arrays†

Slavoj Kresák,*[ab] Tibor Hianik[b] and Renate L. C. Naumann*[a]

Received 16th April 2009, Accepted 30th June 2009
First published as an Advance Article on the web 10th August 2009
DOI: 10.1039/b907661a

A robust platform providing a fluid lipid bilayer is in great demand not only for specific basic research on membrane proteins, but also for related applications. Here we present electrically sealing solvent-free bilayer lipid membranes spanned over arrays of cylindrical nanopores. The nanopores are milled through thin Si_3N_4 diaphragms using a focused ion beam (FIB). Scanning electron microscopy (SEM) and atomic force microscopy (AFM) reveal pores with regular shapes and inter-pore spacing. Nanopore-spanning bilayer lipid membranes (npsBLMs) are formed reproducibly by directed fusion of giant unilamellar vesicles (GUVs) to the pore-containing diaphragms. The arrays of npsBLMs exhibit electrical resistances in the GΩ range, lifetimes of up to several days, and breakdown voltages above 250 mV. Perfusion robustness of the npsBLMs and low aspect ratio of the nanopores allow easy access to both sides of the bilayers. npsBLM conductance in the presence of the pore-forming toxin gramicidin D increases depending on the concentration levels. Peptide-to-lipid molar ratios can reach as high as 1 : 23. Recordings of ionic currents through alamethicin channels are possible with single-channel resolution after dielectric passivation of the substrates. This demonstrates the applicability of the platform to biophysical research of membrane proteins as well as pharmaceutical drug screening assays.

1 Introduction

Attempts have been made in the past decade to develop free-standing bilayer lipid membranes (BLMs) over micrometre or nanometre sized pores.[1–7] The principle aim of these studies was to overcome the drawbacks of the classical BLM, such as low stability and difficulties in preparation, and to arrive at a robust bilayer architecture amenable to automation and sensor development. Unfortunately, an increase in BLM stability by reduction of aperture size comes at the expense of diminished BLM area. Reconstitution of a sufficiently high number of proteins may be difficult. Multiple adjacent pores of small diameters all spanned by BLMs resolve the problem: a large enough total BLM area is attained, while overall stability is preserved. In addition, individually addressable multiple BLMs in a single device are a prerequisite for drug screening assays. With this prospect in mind, BLMs were spanned over arrays of micro-apertures in polymer septa[2–4] and multiporous materials with submicrometre pore width, namely anodized porous silicon[8,9] and alumina.[10,11] Similarly, successful formation of BLMs has been reported on porous silicon nitride[12] and polymer[13] substrates fabricated by means of micro-device technology. These BLMs, also termed micro- and nano-BLMs, were prepared by the Mueller–Rudin technique,[14] *i.e.* 'painting' of a lipid solution over the pores, which introduces solvents such as *n*-decane into the bilayer. Organic solvents, however, may affect the physical and structural properties of the lipid environment and thus alter the behavior of proteins or peptides under study. Moreover, functional reconstitution of complex proteins into micro- and nano-BLMs has not been reported so far.

For these reasons, attention has moved toward solvent-free BLMs, which can be formed by spreading/fusion of (proteo)lipid vesicles. As opposed to painted BLMs, a vesicle-derived nanopore-spanning BLM (npsBLM) is completely free of organic solvents. Unlike a patch-clamp of cells, it allows for precise control of membrane composition. Artifacts related to the presence of variant channel and/or pore species in the patch are thereby eliminated. In addition, an npsBLM offers an elegant way to reconstitute transmembrane proteins directly upon membrane formation, thus avoiding the most critical step of membrane protein research in artificial matrices. Functional reconstitution of complex proteins into preformed BLMs proved to be challenging.[15] A native tissue preparation in which protein activity is fully preserved is, on the other hand, often predominantly composed of proteovesicles that may be employed in npsBLM formation. In addition, numerous protocols for functional reconstitution of delicate proteins into liposomes of a desired lipid composition have been developed.[16]

npsBLMs formed from vesicles on surfaces with ordered cylindrical *blind* pores were investigated previously.[17–20] Unfortunately, low-resistance electrical access to the bilayers is possible only if suitable electrodes are present inside the cavities.[13] In addition, the medium filling the cavities is not accessible unless the

[a]*Max Planck Institute for Polymer Research, Ackermannweg 10, 55128 Mainz, Germany. E-mail: naumannr@mpip-mainz.mpg.de; kresak@mpip-mainz.mpg.de*
[b]*Department of Nuclear Physics and Biophysics, Faculty of Mathematics, Physics and Computer Science, Comenius University, Mlynská dolina F1, 842 48 Bratislava, Slovakia*

† Electronic supplementary information (ESI) available: Additional experimental methods (section S1) and a detailed electrical scheme of a Si_3N_4 TEM window (section S2). See DOI: 10.1039/b907661a

npsBLMs are disrupted. Unlike blind pores, *through* pores do not suffer from such access limitations. Fluorescence and atomic force microscopy showed that npsBLMs can be spanned over through nanopores in multiporous substrates by fusion/rupture of vesicles[21,22] or adhesion of cell membrane fragments.[23] Spanning all of the pores of such a multiporous substrate can be a problem. Full coverage is a prerequisite for dc electrical measurements at low noise and low background currents, however. Good sealing resistances were obtained for npsBLMs from giant unilamellar vesicles (GUVs) over single pores in silicon nitride diaphragms[24] and glass cover slips.[25] In both cases, though, the pore size was in the micrometre range, and there was little control over the process of bilayer formation. Moreover, the presence of charged lipids in the GUV lamella was required in the work of Schmidt *et al.*[24] Sealing npsBLMs derived from large unilamellar vesicles (LUVs) were formed recently over through nanopores in Si_3N_4 diaphragms.[22] Again, however, only diaphragms with single pores were used for current measurements, and the peculiarities of the setup (*e.g.* a non-faradaic AFM tip holder as an electrode) did not allow for standard electrophysiological recordings. Most recently, formation of npsBLMs from LUVs over functionalized porous alumina has been explored.[26] Although a substantial increase in substrate resistance was observed, the GΩ range has not been attained on these multiporous substrates. As pointed out by the authors, the remaining conductance was most likely due to incomplete pore coverage with bilayers.

In the above studies, formation of npsBLMs from vesicles was impaired by a high degree of randomness. As a result, npsBLMs were formed by chance. This made it particularly difficult to span all of the exposed pores. In contrast, we made use of directed fusion of GUVs over nanopores in the Si_3N_4 diaphragms. Directed fusion refers to spreading and rupture of GUVs under optical and mechanical control (Fig. 1). Solvent-free electrically sealing lipid bilayers are thus obtained in a highly controllable fashion. This method made it possible for the first time to prepare giga-seal lipid bilayers spanning over *arrays* of through pores. Maneuvering of GUVs to the localized arrays almost always spans all pores with npsBLMs. We find that the npsBLMs so-formed exhibit temporal stability for up to several days. Moreover, they can withstand continuous perfusion and high osmotic gradients, which allows for easy exchange of electrolyte and delivery of arbitrary compounds. Since the nanopores exhibit a low aspect ratio, access to the bilayers through the pores does not suffer from diffusion limitations in confined geometries. Electrical resistances in the range of 10^{10} Ω are obtained reproducibly. Dielectric properties of the Si_3N_4 window can additionally be tailored by applying a photoresist resin. Such a combination of properties makes the npsBLMs described here a very attractive platform for the development of pharmaceutical screening assays and biosensor devices based on the detection of low ionic currents through protein channels or pores. We demonstrate this potential by monitoring gramicidin-induced

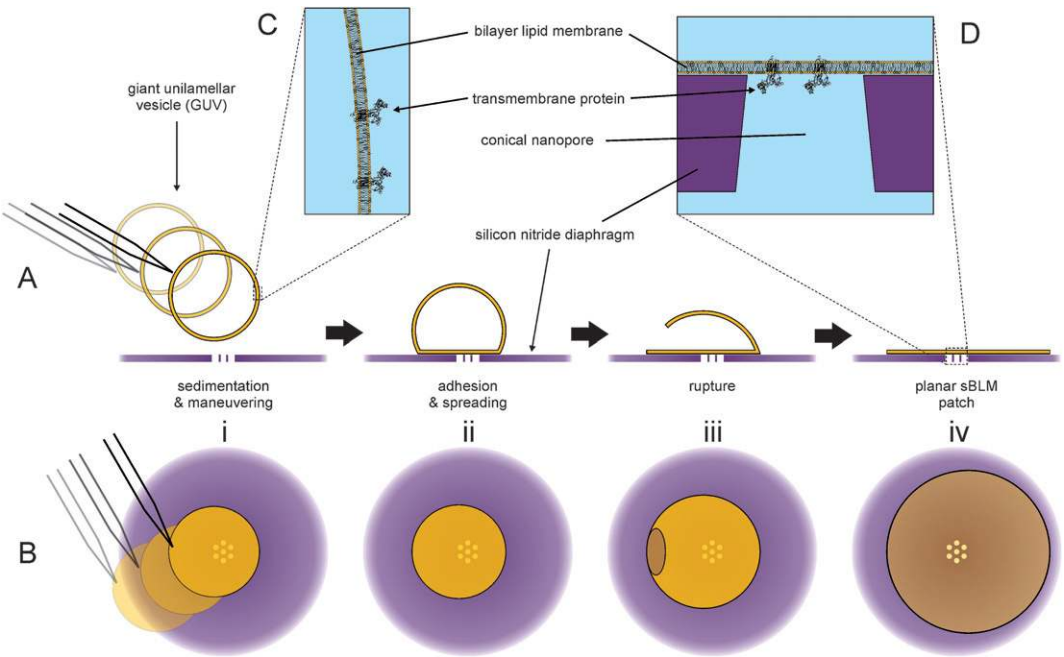

Fig. 1 Schematic of npsBLM formation by directed fusion of a GUV to a Si_3N_4 diaphragm containing an array of pores (not drawn to scale, except for D). (A) and (B) are side and bird's-eye views of the formation process, respectively. (i) GUV suspension is injected in the bathing electrolyte and GUVs sediment to the Si_3N_4 diaphragm. One of the GUVs sinking at the pore-bearing location is maneuvered to directly above the pore array by horizontal movements of a patch pipette tip attached to a micromanipulator. (ii) Upon contact with the Si_3N_4 diaphragm, the GUV adheres to the surface and spreads into a pancake-like shape, spanning over all pores of the array. (iii) A spontaneous local loss of integrity of the lipid bilayer, *i.e.* rupture, occurs at the rim of the GUV as it flattens on the surface. The defect widens progressively as the vesicle unfolds. (iv) The GUV unfolds completely, forming a large planar sBLM patch spanning all pores of the array. (C) A zoom-in at the GUV lamella, displaying in detail the lipid bilayer with reconstituted transmembrane protein. (D) A zoom-in at an npsBLM spanning a slightly conical nanopore 50 nm wide and 50 nm long (drawn to scale).

conductivity by ac measurements and detection of dc currents through alamethicin channels with single-channel resolution.

2 Materials and methods

2.1 Reagents and materials

Lipids 1,2-diphytanoyl-*sn*-glycero-3-phosphocholine (DPhPC) and *N*-(7-nitrobenzoxa-2,3-diazol-4-yl)-dimyristoyl-phosphoethanolamine (NBD-DMPE) were purchased from Avanti Polar Lipids (Alabaster, AL, USA). Gramicidin D and alamethicin were purchased from Sigma-Aldrich (Taufkirchen, Germany) and Serva (Heidelberg, Germany), respectively, and used as received. The water used was ion-exchanged and filtered with a Milli-Q-System (Millipore, Molsheim, France; specific resistance $R > 18$ MΩ cm, pH 5.5). KCl, $N(CH_3)_4Cl$ (TMACl), $N(CH_3)_4OH$ (TMAOH) and HEPES, all of >99% purity, were purchased from Sigma-Aldrich. Unless otherwise noted, electrolytes were adjusted to pH 7 by TMAOH and buffered by 5 mM HEPES. All solutions were filtered through 0.2 μm pore size Rotilabo nylon syringe filters (Carl Roth GmbH, Karlsruhe, Germany).

2.2 Si_3N_4 TEM window parameters and pre-treatment

Silicon nitride transmission electron microscopy windows (Si_3N_4 TEM windows) were used as substrates in this study. A Si_3N_4 TEM window is a square-shaped piece of a silicon wafer coated on both sides with a thin layer of silicon nitride (Fig. 2A). A pyramidal pit has been etched through the entire thickness of the chip from one side. The exposed unsupported square-shaped part of the Si_3N_4 film on the other side is referred to as the 'Si_3N_4 diaphragm'. Si_3N_4 TEM windows of the following nominal parameters were purchased from Silson Ltd. (Northampton, England): Si frame thickness 525 μm, Si frame width 5 × 5 mm, Si_3N_4 diaphragm thickness 100 nm, Si_3N_4 diaphragm width 250 μm. The actual Si_3N_4 diaphragm width was 330 μm, as determined by both SEM and light microscopy. Prior to pore machining, a 10 nm layer of Au was evaporated over the 'pit' side of the TEM window to avoid local charge accumulation upon focused ion beam (FIB) machining and SEM imaging. After pore fabrication, the Au layer was dissolved in aqua regia (a 3 : 1 mixture of 37% HCl and 68% HNO_3).

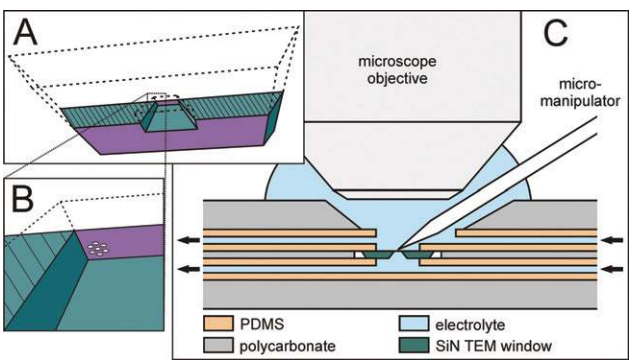

Fig. 2 (A) 3D section view of a TEM Si_3N_4 window. Note the pyramidal pit in the center. (B) Zoom-in at the pore-bearing corner of the Si_3N_4 diaphragm. (C) Section view of the cell used for the formation and electrical investigation of npsBLMs on porous Si_3N_4 TEM windows (drawn to scale, TEM window width is 5 mm). The Si_3N_4 TEM window is mounted in the center. Both sides of the window are accessible to perfusion by inlet and outlet channels, as indicated by the arrows. The top side can additionally be accessed optically by the immersed microscope objective and mechanically by the micromanipulator tip.

2.3 Fabrication and imaging of nanopores

The focused Ga^+-ion beam of the DualBeam™ Nova 600 NanoLab (FEI Company, Hillsboro, OR, USA) nanotechnology device was used to mill circular nanopores through the thin free-standing Si_3N_4 diaphragms of the TEM windows. An array comprising 3–12 pores of 50–200 nm in diameter or a single pore of 50–600 nm in diameter was milled per diaphragm. Scanning electron microscope (SEM) images of the FIB milling site on the TEM windows were acquired by detection of secondary electrons induced by the electron beam of the Nova 600 NanoLab. The topography of the pore openings at the flat side of the TEM windows was examined using an atomic force microscope (AFM) in the tapping mode with the Dimension 3100 AFM (Veeco Metrology Inc./Digital Instruments, Santa Barbara, CA, USA) with OMCL-AC160TS-W2 silicon cantilevers (Olympus Corp., Tokyo, Japan). Topography bitmaps were captured and pre-processed using the Nanoscope v7.2 software. Pore sizes were determined by image processing and analysis (ImageJ, GIMP) of secondary electron emission and height bitmaps acquired by SEM and AFM, respectively.

2.4 Formation of npsBLMs

Prior to npsBLM formation, a pore-bearing TEM window was cleaned for 10 min in a fresh piranha solution. Next, the TEM window was mounted horizontally in the cell (Fig. 2) with the flat side facing upwards. Electrolyte was introduced into both compartments by perfusion channels. The cell was mounted on the stage of an upright DIC microscope, an objective was immersed in the top compartment, and the pore-bearing region of the Si_3N_4 diaphragm was localized. The stage was lowered and a micromanipulator tip was brought into view, focused, centered, and raised slightly so as not to collide with the free-standing Si_3N_4 diaphragm. The objective was withdrawn and 0.5–2 μl of a GUV suspension was injected by a micropipette. The objective was re-immersed and the pore-bearing region brought into focus. The micromanipulator tip was lowered to ~10 to 20 μm above the surface. One of several GUVs that typically sank to the vicinity of the pore array was maneuvered to and centered over the array by lateral movements of the manipulator tip (Fig. 1). The GUV was then allowed to adhere, spread and unfold over the pore-bearing location. A supported bilayer lipid membrane (sBLM) patch was formed over the Si_3N_4–electrolyte interface and npsBLMs over the pores. The top compartment was flushed with base electrolyte to remove sucrose and lipid debris suspended in the solution, and to verify npsBLM stability. Electrolyte was exchanged and pore-forming peptides were introduced by perfusion of the chambers either manually through tubing connected to disposable syringes or using a Reglo ISM834 peristaltic pump (Ismatec SA, Glattbrugg, Switzerland).

2.5 Electrical measurements

Electrical measurements were carried out by means of two AgCl-coated Ag wires. The electrodes were sealed in the PDMS matrix of the measurement cell and communicated with the electrolyte in the respective compartments by perfusion channels. Impedance spectra of the free pores and npsBLMs and ac current *vs.* time traces at constant frequency were recorded using an Autolab PGSTAT302 (Eco Chemie B.V., Utrecht, The Netherlands) expanded with an FRA2 frequency analysis module and controlled from the FRA 4.9.007 software (Eco Chemie). Impedance spectra were measured for frequencies between 2 mHz and 20 kHz at 0 V bias potential with an RMS ac modulation amplitude of 10 mV. 200 mHz, a compromise between sufficient time resolution and npsBLM resistance sensitivity, was typically used for the ac current *vs.* time recordings at a constant frequency. Equivalent circuit parameters were fitted to the experimental data in ZView 2.8 software (Scribner Associates, Southern Pines, NC, USA) using a non-linear least squares algorithm. Single-channel currents were recorded by means of an EPC10 patch-clamp amplifier (HEKA Elektronik Dr. Schulze GmbH, Lambrecht/Pfalz, Germany). The signals were filtered at 3 kHz by a built-in low-pass Bessel filter. The EPC10 amplifier was controlled by Patchmaster 2.1 software (HEKA). Data were analyzed and plotted in Origin 8 software (OriginLab Corp., Northampton, MA, USA).

For details on the fabrication of nanopores by FIB, preparation of GUVs, imaging of GUVs and sBLMs by light microscopy, and TEM window passivation, see section S1 of ESI†.

3 Results and discussion

3.1 Nanopore size, distribution and topography

Fig. 3a shows an SEM image taken at a 65 000× magnification of an array of seven pores in a 100 nm thick silicon nitride diaphragm. All pores are clearly resolved as circles of low signal intensity (no secondary electrons induced) against the gray continuous Si_3N_4 diaphragm (some secondary electrons induced). The obvious white islets scattered over the surface are regions of the diaphragm covered with gold (high secondary electron yield). Gold films are known to coagulate during growth on silicon-derived substrates.[27] At an average layer thickness of ~10 nm, the islets are interconnected in a partly closed layer, as visible at the periphery of the image. In the vicinity of the pores, however, the white patches are scarce, small and isolated. Apparently, a considerable portion of the Au layer has been etched off this region during the pore milling process. For the specific array, particle analysis after image processing yields for the distal pore opening an average diameter of 183.7 ± 2.2 nm (200 nm nominal) and the nearest center-to-center distance of 497.5 ± 2.2 nm (500 nm nominal). A contour of a wider proximal pore opening, ~220 nm in diameter, can be noted at each pore. Slopes of features milled vertically through a continuous material by an FIB are known to deviate from the normal.[28,29] Apparently, the pores exhibit the shape of truncated cones rather than cylinders, with a taper of ~12°.

Fig. 3b displays a planar AFM height scan of the flat side of the same array, the pit side of which is depicted in Fig. 3a. The pores appear as regular depressions against the flat continuous

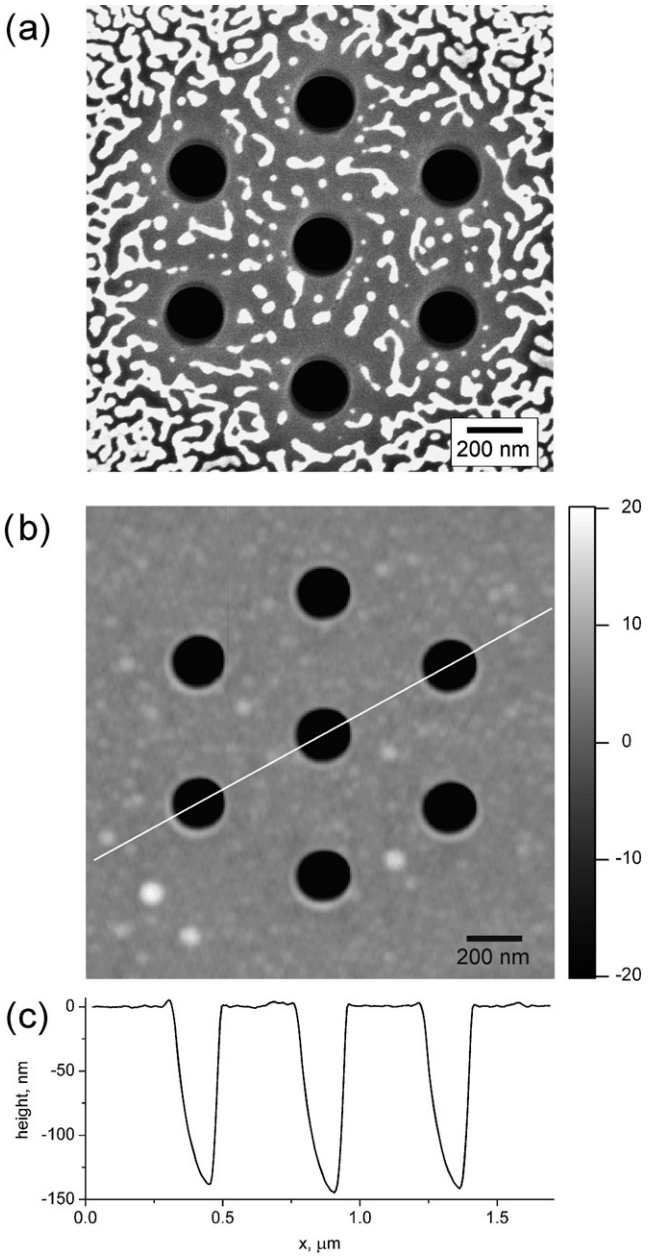

Fig. 3 SEM (a) and AFM (b) images of the 'pit' and the 'flat' side, respectively, of a 7-pore array milled through a 100 nm thick Si_3N_4 diaphragm by FIB. The nominal pore diameter and center-to-center distance were 200 nm and 500 nm, respectively. (b) Unit of the height bar is nm. (c) Height profile along the white line depicted in (b).

Si_3N_4 membrane. Apart from a few circular elevated spots, the Si_3N_4 membrane itself is considerably smooth. Average roughness, Ra, of ~0.8 nm has been determined for analogous Si_3N_4 surfaces free of pores (images not shown). Similar to SEM, the pores imaged by the AFM have a well-defined circular shape. Although slight distortion of AFM images due to lateral drift of samples in the course of capture was often observed, the topographical information remained unaffected. Fig. 3c is a profile scan along the line depicted in Fig. 3b. The asymmetric quasi-conical profile and finite depth of the pores are AFM imaging artifacts. AFM reveals elevations of up to 10 nm in height along

sections of pore edges (faintly brighter annuli in Fig. 3b, an elevation at $x = 0.3$ μm in Fig. 3c). Such rim-like features of varying height and continuity appeared irregularly along the pores. Their existence seems to be related to specific parameters set for the FIB pore fabrication procedure.

Arrays constituted of 3–12 pores of 50–200 nm in diameter exhibited overall available pore areas in the range of 0.006 to 0.4 μm^2; the areas of single pores in the range of 50 to 600 nm in diameter were 0.002–0.3 μm^2. The total areas of our larger arrays match those of the single pores used by White *et al.* (100–800 nm in diameter, areas up to 0.5 μm^2),[30] and the smaller single pores used by Schmidt *et al.* (0.6–7 μm in diameter, 0.3–40 μm^2)[24] and Fertig *et al.* (1–2 μm in diameter, 0.8–3 μm^2).[31] The total areas of our arrays can be easily expanded by increasing the number of pores comprised therein.

3.2 Resistance of unobstructed pores

The resistance of an individual cylindrical pore filled with electrolyte, R_p, can be correlated with the pore dimensions by $R_p = (R_{flat} + R_{internal} + R_{pit})$, where $R_{flat} = 1/4\kappa r_{flat}$, $R_{internal} = l_p/(\pi\kappa r_{flat} r_{pit})$ and $R_{pit} = 1/4\kappa r_{pit}$.[32–36] In these expressions, κ stands for electrolyte conductivity, r_{flat} and r_{pit} are the radii of the pore openings at the respective sides of the Si_3N_4 membrane, and l_p is the length of the pore. Electrochemical impedance spectra were thus acquired for Si_3N_4 membranes with varying pore size and number. Resistance of free unobstructed pores, as well as the overall electrical parameters of the system, was evaluated using a model circuit discussed below. Fig. 4 displays the measured and theoretical single pore resistance, R_p, with respect to pore size. In the case of single pore TEM windows, R_p is equal to the measured resistance, R_P. In the case of TEM windows with pore arrays, R_P was corrected for the number of pores, n, in the diaphragm: $R_p = nR_P$. Only multi-pore TEM windows with a constant nominal diameter for all pores per window were included. Experimental data presented as scattered points for 100 mM TMACl, 100 mM KCl and 1 M KCl (all of pH 7, buffered by 5 mM HEPES) are overlaid with the theoretical pore resistance traces. In the theoretical calculations based on the equation above, l_p was 100 nm, as given by the thickness of the Si_3N_4 membrane, κ was 1.282 S m^{-1} and 10.86 S m^{-1} for 0.1 M and 1 M KCl,[37] respectively, and 0.969 S m^{-1} for 0.1 M TMACl.[38] r_{flat} was substituted by nominal pore radius. r_{pit} was determined from r_{flat} by correcting for the truncated cone taper obtained from SEM image analysis. A taper independent of pore width was assumed. The experimental pore resistance data were well distributed along the corresponding simulated curves for the given range of pore radii. Discrepancies might be the result of a mismatch between nominal and actual pore size, which has not been accounted for in the figure. Moreover, assuming an electrolyte conductance temperature coefficient of ~2%, room temperature fluctuations might have given rise to ~10% scatter interval of the measured pore resistances.

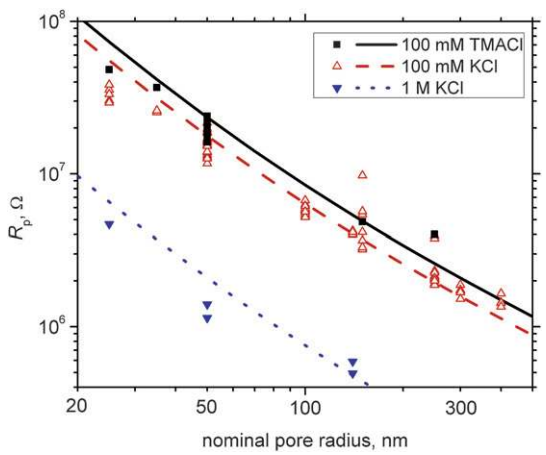

Fig. 4 Experimental and theoretical resistance, R_{IP}, of a single unobstructed pore in a Si_3N_4 diaphragm milled by FIB. Scattered points represent experimental data, solid lines are theoretical curves for single 100 nm long cylindrical pores. Data measured and calculated for 100 mM TMACl, 100 mM KCl and 1 M KCl are shown (see legend). All electrolytes were buffered by 5 mM HEPES at pH 7.

3.3 Adhesion, spreading and rupture of GUVs on Si_3N_4 surfaces

In order to be able to suspend npsBLMs over nanopores it is essential that defined sBLMs rather than multilayers or even layers of adsorbed vesicles are formed on the surface surrounding the pore. To achieve this goal, vesicles must fuse and rupture in a controlled way to form sBLMs that are able to stabilize the npsBLM. Liposomes are known to form sBLMs on hydrophilic surfaces including Si_3N_4.[39] Therefore, the behavior (fusion and rupture) of fluorescently labeled giant vesicles was first followed *in situ* on plain Si_3N_4 surfaces without pores.

The method of npsBLM formation presented in the following makes use of sedimentation of GUVs through an aqueous medium to the Si_3N_4 surface of a TEM window. Sedimentation is achieved by a density gradient between the internal medium of the GUVs (200 mM sucrose) and the base electrolyte (100 mM KCl, 5 mM HEPES, pH 7) while keeping the vesicles under an osmotic equilibrium. The osmotic equilibrium prevents vesicles from rapid leaking or swelling that might likely lead to a collapse of the vesicular structure soon after injection in the electrolyte. Collapse in the course of sedimentation would clearly reduce the number of vesicles available for npsBLM formation. Although the vesicles might be able to avoid collapse by release of osmotic stress *via* transient pore formation in the lamella, mixing of the internal and external contents would inevitably be induced. This way, the optical contrast given by the different refractive indices of the inside and outside would be lost, and the vesicles would no longer be resolvable in the standard modes of optical microscopy.

After injection into the medium the GUVs were observed to sink to the Si_3N_4 surface. Their behavior at the interface was strongly dependent on the ionic content of the electrolyte. Unless the concentration of cations in the medium was very low, the vesicles followed a sequence of adsorption, spreading, and spontaneous rupture at the surface, forming patches of planar supported lipid bilayers, as observed previously.[40–42] Low pH and divalent cations enhanced the rate at which the transition from vesicular to planar form occurred.[43]

Fig. 5 is an overlay of two fluorescence microscopy images. The *red* layer depicts a group of GUVs adhered and partly spread over a Si_3N_4 surface. Although the planar projections of most of

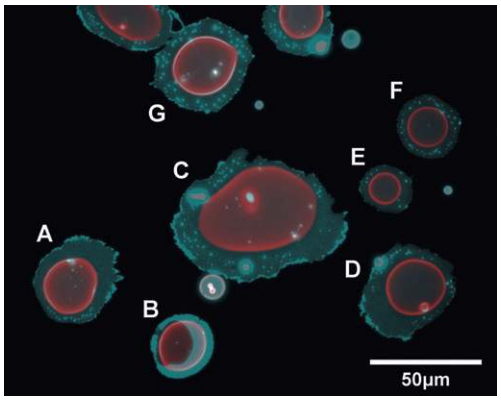

Fig. 5 Fluorescence images of GUVs adsorbed on a continuous Si_3N_4 surface (red), and patches of sBLMs formed by the rupture thereof (cyan).

the vesicles in the figure are near to circular (*e.g.* GUVs A, B, D–F) distortions of shape upon spreading, such as that of vesicle C, were commonly observed. The intensity of the fluorescent signal is minimal in the central area and peaks at the edge of a vesicle. This is a typical outcome of imaging transparent surface-labeled 3D objects *via* a conventional fluorescent microscope. The *cyan* layer of Fig. 5 shows planar sBLM patches formed by rupture of the corresponding GUVs. The area of the patches complied well with the surface area of the vesicles, as estimated from their diameter before the transition. This result gave strong evidence that the patches bear predominantly a bilayer structure and can indeed be referred to as sBLMs.

3.4 Impedance changes during npsBLM formation

In order to form npsBLMs over nanopores, we used the same sedimentation procedure as described in the last paragraph. In addition, on a porous substrate, single GUVs were maneuvered to above the pore(s) by lateral movements of the tip of a patch-clamp pipette, which was directed under the microscope objective by a micromanipulator (Fig. 1). Adsorption and fusion of GUVs were thus performed under visual and electrical control. The evolution of electrical properties of the assembly was determined by impedance spectroscopy.

GUV adhesion to the surface of a Si_3N_4 membrane over a pore was detected as a fall of admittance of the Si_3N_4 TEM window to below 1 nS, as monitored in the continuous ac current *vs.* time mode at 0.2 Hz. Fig. 6a displays a conductance trace with respect to time of an npsBLM forming over a single 300-nm-wide pore in 100 mM TMACl base electrolyte. The trace starts just below 250 nS, *i.e.* at a conductance level that complies well with what is expected for the particular pore parameters and electrolyte composition. After injection of 1 μl of a GUV suspension, real admittance exhibits a fall to ~140 nS followed by a logarithmic-like climb. The drop is attributed to the dense sucrose suspension sinking to the bottom of the compartment and locally changing the electrolyte composition. The subsequent climb is an effect of a slow diffusion-driven restoration of the original ion concentration at the Si_3N_4–liquid interface. During this period a GUV has been maneuvered to above the pore by the micromanipulator tip. Its adhesion and rupture at time 150 s are accompanied by

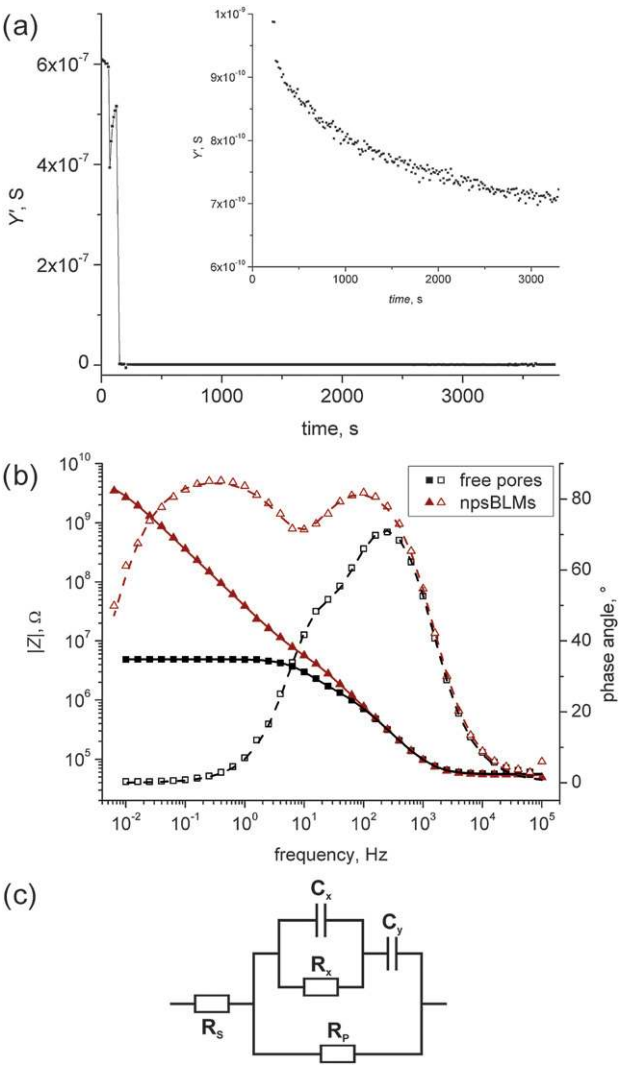

Fig. 6 Formation of npsBLMs monitored by impedance spectroscopy. (a) Real component of admittance *vs.* time trace derived from a continuous ac current recording (10 mV rms, 200 mHz). GUVs were injected 70 s and the npsBLMs formed 125 s after the start of the recording, repectively. The inset displays the same trace at a finer scale. (b) Bode plot of impedance spectra taken before and after npsBLM formation. Scattered points represent experimental data (|*Z*|—solid symbols, phase—open symbols), lines are the best-fit traces modeled using an equivalent circuit drawn in (c).

a fall of pore conductance to below 1 nS (inset of Fig. 6a). Typically, it would take the GUV a few seconds to spread, rupture and form a planar sBLM patch, but could also take up to 2 h for the complete process in some cases. The spreading phase and the rupture were not observed to have an additional impact on the ac conductance of the covered pore(s). Bode plots of impedance spectra of the TEM window with an open and npsBLM-covered pore acquired before and after the Y' *vs.* time trace (Fig. 6a), respectively, are shown in Fig. 6b. Before GUV adhesion, the pore resistance of 4.9 MΩ clearly dominates the part of the spectrum below 2 Hz, with the phase angle converging all the way to 0 at 100 mHz. After npsBLM formation over the pore, the resistance shoots up by 3 orders of magnitude to 7.6 GΩ, as clearly revealed by the capacitive dominance over the

same part of the spectrum. The onset of resistive convergence of $|Z|$ barely becomes apparent before the lowest frequencies are reached.

All impedance spectra, except those acquired for photoresist-coated TEM windows, were interpreted in terms of the circuit depicted in Fig. 6c. R_P and R_S correspond to the resistance of the pore, or array of pores, and the combined resistance of electrolyte and electrodes, respectively. After a lipid bilayer has been spanned over the pores, R_P reflects the resistance of the npsBLMs. The overall capacitance of bilayers spanning our largest pore arrays ($\sim$0.4 μm^2) is below 10 fF, which is negligible relative to the (parallel) capacitance of the TEM window ($\sim$2 nF untreated, $\sim$50 pF passivated). Bilayer capacitance is thus not considered in the modeling scheme. R_x, C_x, and C_y are the circuit components that account jointly for the contribution to the impedance of the native SiO_x and the space-charge (SC) region of the pit walls, as well as the layers of Si_3N_4 on both sides of the TEM window. The circuit used for routine modeling (Fig. 6c) is a simplification of a fully detailed circuit that takes every section of the TEM window into account individually (see section S2 of ESI†). Fitting accuracy provided by the detailed and the simplified circuit is equivalent. As R_P is the only parameter extracted from the fits, the use of the simplified albeit physically less straightforward circuit is justified. Impedance of native SiO_x and the SC region is linked to the open circuit potential (OCP) of the bulk semiconductor,[44,45] which in our case is the Si of the window frame. Our parallel experiments show that under the particular experimental conditions the OCP rises in time convergently in the range of -300 mV to +50 mV *vs.* Ag/AgCl (results not shown). The dynamics of R_x, C_x, and C_y due to this temporal drift of the OCP of the frame manifests as shifts of impedance spectra in the 1–1000 Hz interval (*e.g.* Fig. 8). These shifts do not interfere with or obscure the low-frequency part of the spectra dominated by R_P.

Formation of npsBLMs by directed fusion of GUVs was highly reproducible. With some manipulation practice, a success rate of $\sim$90% has been attained. Overall, total seal resistances of hundreds of MΩ up to several tens of GΩ were obtained for npsBLMs formed over single as well as multiple nanopores. This range is comparable to that reported earlier for single npsBLMs formed by rupture of GUVs carrying a negative charge on their envelopes over pores in positively charged SiO_2/Si_3N_4 diaphragms.[24] A similar variation of seal resistance has been found for BLMs spanned over single nanopores in glass.[34] No apparent dependence of npsBLM resistance on pore size or sBLM patch size (estimated from the size of the GUV giving rise to the sBLM patch) has been observed in this study. Intriguingly, npsBLM resistance was observed to vary not only among samples, but also with respect to repeated tries using the same TEM window. In general, npsBLMs formed over Si_3N_4 surfaces that were rinsed briefly with water and ethanol without cell disassembly showed lower seal resistances as opposed to npsBLMs formed over surfaces treated with a fresh piranha solution. The npsBLMs were able to withstand continuous bilateral perfusion. This provided a convenient pathway to change the composition of the bathing electrolyte or to insert pore-forming peptides. The need for stirring as well as errors and lags arising from uneven distribution of substances in the electrolyte compartment upon injection was thus avoided.

3.5 npsBLM breakdown voltages

An important criterion of the stability of an npsBLM is the temporal breakdown of the resistance due to the application of defined potentials. Characteristic breakdown voltages of classical BLMs are in the range of 150 to 200 mV.[46] Breakdown voltages of npsBLMs formed by controlled fusion of GUVs were tested by sweeping dc potential across npsBLM arrays at low scan rates (10–20 mV s^{-1}). This approach allowed for the isolation of individual bilayer breakdown events. The system exhibits ohmic behavior, *i.e.* upon a linear potential sweep the slope of the current trace is equal to the total conductance, G_{total}. The total current through an array of unobstructed pores is given by the sum of currents through the individual pores: $I_{total} = \sum I_{IPi}$, where $I_{IPi} = V/R_{IPi}$ and R_{IPi} is the resistance of an individual pore. If the pores composing an array exhibit constant length and width, every unobstructed pore contributes an equal share to the total current: $I_{total} = nI_{IP} = nV/R_{IP}$, where n is the number of unobstructed pores. A single npsBLM collapse, *i.e.* a pore opening event, increases the current by $I_{IP} = V/R_{IP}$, and the total conductance becomes $G_{total} = n/R_{IP} + 1/R_{IP} = (n + 1)/R_{IP}$. Individual opening events of pores of equal dimensions can thus be detected as discrete conductance leaps, $\Delta G = 1/R_{IP}$.

An instance of current traces recorded in response to linear dc potential sweeps across an array of npsBLMs is displayed in Fig. 7a. The measurement was performed in a TMACl electrolyte using a 12-pore array of 100 nm nominal pore width and 1 μm center-to-center distance. A unit cylindrical pore conductance of about 43 nS is predicted by theory (*vide supra*). A single npsBLM collapsed before the measurement began, thus the current slope between 0 and 290 mV of the 1st sweep reflects the conductance of a single open pore. At 290 mV a single npsBLM collapse occurs accompanied by an instantaneous current leap to about twice the previous magnitude. The new conductance level corresponds to 2 unblocked pores. For the rest of the sweep, *i.e.* up to the reversal potential of 300 mV and back to 0 mV, the current trace follows the doubled system conductance. The ascending current trace of the next sweep overlays the descending trace of the former sweep, indicating the number of conductive pores has not changed. At 260 mV the current leaps to yet another level due to the opening of the 3rd pore. The successive current traces portray the breaking of the rest of the npsBLMs in the same fashion. Note that the collapse of the 4th and 5th, 8th and 9th, and 10th and 11th npsBLM occurred shortly after each other in the scope of the same respective potential sweeps. The 'skipped' conductance levels (4, 8, and 10 open pores) could hence not be resolved.

Conductance (extracted *via* impedance spectra modeling) with respect to the number of open pores is plotted as scattered points in Fig. 7b. A fit of a linear equation (*solid line*) to the experimental data generates a unit pore conductance of 52.2 ± 0.7 nS. Only a negligible discrepancy exists between the final resistance after all 12 npsBLMs were broken (1.66 MΩ) and the initial resistance measured before the npsBLMs were formed (1.69 MΩ, *open triangle* in Fig. 6b). Apparently, the residues of the npsBLMs after collapse that might possibly be covering sections of pore walls did not make an impact on free pore resistance.

Fig. 7c displays a plot of breakdown voltage against the breaking event sequence number. A general rising trend can be

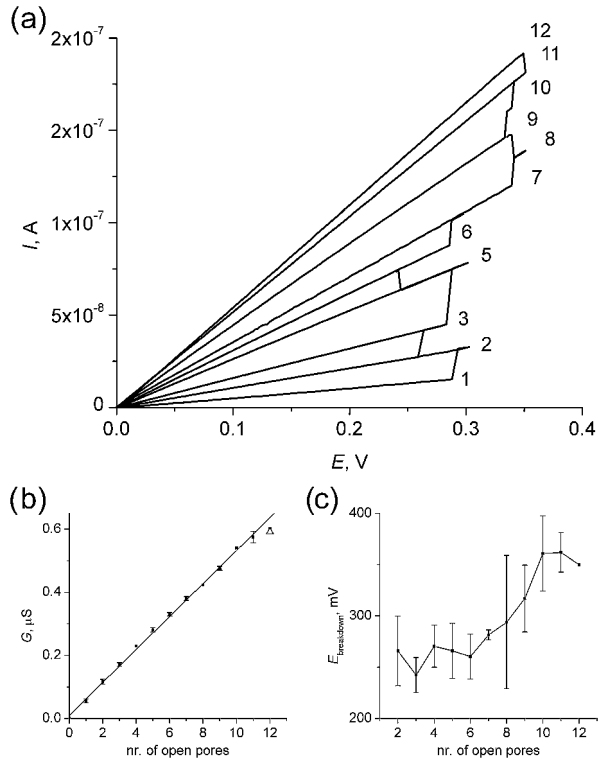

Fig. 7 npsBLM breakdown at elevated dc potentials. npsBLMs were suspended over a 12-pore array of 100 nm nominal pore width and 1 μm center-to-center distance. Potential across the TEM window was swept linearly between 0 mV and a variable positive reversal value at a rate of 10 mV s^{-1}. Single and double npsBLM breakdown events were observed. (a) Current traces corresponding to the successive potential sweeps. Conductance of the partition is defined by the steady-state current gradient. npsBLM breakdown events appear as rapid transitions to higher conductance levels in the potential range of 240–350 mV. The figures to the right denote the number of open pores per particular conductance level. (b) Conductance *versus* number of open pores (scattered points) and a linear fit thereof (solid line). Conductance of the TEM window prior to npsBLM formation is represented by the open triangle. (c) Breakdown potential with respect to the sequence number of the breaking event. Data plotted in (b) and (c) come from two independent experiments on the same array.

noted which indicates that either (1) a variation in robustness exists among the individual npsBLMs irrespective of the state of the neighboring suspended bilayers or (2) the effect of the electric field on the remaining npsBLMs weakens as their number decreases. A simple cause of the first alternative might be the presence of heterogeneous topographical features in the vicinity of the pores. No such features were observed *via* AFM after the pores were milled, however. Given the fact that breaking events 3 and 6 occurred at potentials significantly lower than the preceding events, it appears that a breakdown of an npsBLM might at times have a negative influence on the stability of some of the remaining ones. This is contrary to the general validity of the second alternative. At the present time we are unable to characterize the relationship decisively. Our parallel results suggest, however, that the 'sensitivity' of some npsBLMs to the collapse of other npsBLMs in the array seems to get pronounced as the inter-pore distance decreases. Interestingly, downward discrete conductance transitions complying in magnitude with $1/R_{IP}$ were observed in multiple cases on 100 nm wide pores, too. We associate such conductance drops with pore resealing events. It is unlikely that the resealing was due to involvement of lipid structures from the electrolyte, as these had been washed away previously. It appears that the phenomenon is rather related to the dynamics of the sBLM patch itself.

Mayer *et al.*[2] observed breakdown voltages higher than 300 mV for about a half of their BLMs spanned by the Montal–Mueller technique[47] over 50 μm wide apertures in PTFE sheets. In addition, the authors have reported a breakdown voltage of 460 mV using a 2 μm aperture. Ability to withstand dc voltages of up to 780 mV has been reported for painted BLMs spanning nanopores in hydrophobized glass membranes.[30] The breakdown voltages of our npsBLMs are somewhat smaller. The reasons for the difference are not yet fully understood. Breakdown voltages for single pores are reported in these studies, whereas our values refer to pore arrays. The existence of a multitude of pores of low inter-pore distance may have a destabilizing effect on the npsBLMs of the array, as mentioned above. Moreover, due to the existence of an annulus of solvent at the rim of the pore, the actual area of the bilayer region of a painted membrane is difficult to estimate. This may render a direct comparison based on pore size inappropriate. Another aspect to consider is the interactions of phospholipid molecules with the support. In the studies mentioned above the interactions have a hydrophobic character, whereas in our case they are hydrophilic. It might appear plausible that higher stress develops in a BLM suspended by a hydrophilic substrate that would result in bilayer breakdown at lower dc potentials. Recently, however, Mey *et al.* have shown by local indentation of pore-spanning BLMs by AFM tips that BLMs suspended by hydrophilic interactions with the support are less stressed than hydrophobically suspended ones and, unlike the latter, do not rupture even at large indentations.[48] It thus seems that different mechanisms may be involved in mechanically- and electrically-induced npsBLM breakdown.

3.6 Gramicidin D in npsBLMs

Gramicidin D (gD) was used to prove that the lipid assemblies observed to block the conductance of our nanopores are bilayers rather than undefined clogs. gD, a mixture of short bacterial peptides, is known to form ~4 Å wide helical channels in lipid bilayers. A channel is formed by random axial association of two gD monomers each constituting a half-pore through one of the adjacent lipid leaflets. The channels are permeable to ions with a pronounced selectivity toward cations. Ionic flux through the channels is detectable as an electric current.[49]

Fig. 8 shows a sequence of impedance spectra acquired for an npsBLM suspended over a single 280 nm wide pore at varying concentrations of gD in the electrolyte. The trace lined with *open squares* reflects the status of the npsBLM before gD had been introduced, with $R_P \approx 15$ GΩ. The other traces were acquired after stepwise increases of gD concentration in both electrolyte compartments to 320 nM, 1 μM, 3.2 μM and 10 μM, always 1 h after a concentration step was made. The respective pore resistances extracted *via* modeling of the spectra were 133, 91, 61, and 47 MΩ. At 10 μM of gD, an extra spectrum was acquired after 12 h of incubation, revealing a further decrease of R_P to 34 MΩ.

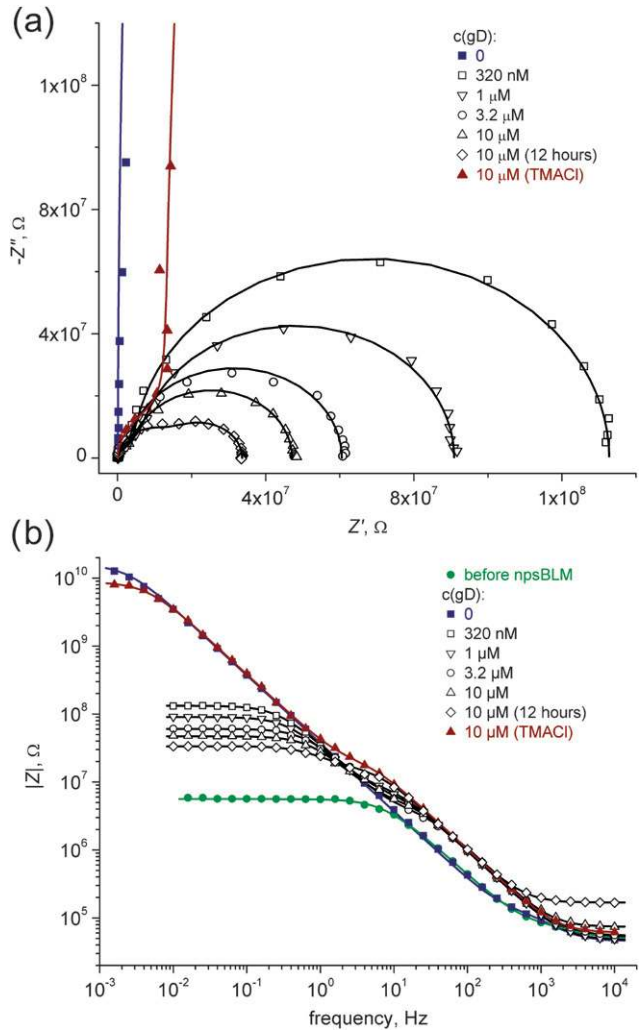

Fig. 8 Nyquist (a) and Bode (b) plot of impedance spectra acquired for a single npsBLM at varying concentrations of gramicidin D (gD). Scattered points represent experimental data (see legend), lines are the best-fit traces modeled using an equivalent circuit drawn in Fig. 6c. The spectrum of a clean chip with a free pore before npsBLM formation has been included in (b) for comparison (open circles).

Apparently, a higher number of conductive gD dimers in the npsBLM had been attained during the additional incubation time.

To rule out the possibility that the observed resistance decline was simply an effect of npsBLM seal deterioration, the base electrolyte (100 mM KCl, 5 mM HEPES, pH 7) was eventually exchanged for 100 mM TMACl, 5 mM HEPES, pH 7, in both compartments. The pore resistance leapt to 8.7 GΩ. gD has been reported to be completely impermeable to TMA^+.[50] The specific conductivity ratio of the two electrolytes is 1.32. Therefore, if some of the conductance could be attributed to a leaky seal, the resistance measured in 100 mM KCl in the absence of gD would not have been restored. Exchange of KCl to TMACl led to a 260-fold increase of resistance, however, to a level near to that before gD addition. This result suggests that the seal deteriorated negligibly in the course of the experiment and the observed increase of npsBLM conductance can indeed be attributed to the presence of gD channels in the bilayer.

Analogous to earlier observations, the presence of gD in the electrolyte induced a concentration-dependent decrease of resistance of the blocked aperture. Given the notion of gD channel formation,[51,52] it is unlikely that an increase of conductance through lipid structures other than bilayers can occur. The observed effect thus indicates that GUV rupture over pore-bearing substrates, as described above, indeed gives rise to pore-spanning lipid bilayers.

Because the attained conductance is rather high with respect to the area of the npsBLM, an interesting question arises as to how much gD was actually present in the bilayer. gD was dissolved in ethanol, diluted in base electrolyte at the desired concentration, and delivered to both sides of the npsBLM by perfusion. gD forms primarily non-conductive double-helical dimers when dissolved in ethanol at high concentrations.[52] These are, however, known to rapidly unwind and break into monomers if the polarity of the solvent is increased (*e.g.* by addition of water in fractional amounts).[53] As the stock solutions of gD in ethanol were mixed with base electrolyte hours prior to administration of the mixture to the bilayer, gD reaching the lipid bilayer was predominantly monomeric. Double-helical dimers are also known to slowly unwind and break into monomers in a lipid bilayer environment.[52] Any residual double helices that did not break apart before having reached the bilayer must have unwound in the course of the lengthy experiment. Therefore, gD is assumed to have resided in the npsBLM in the monomeric or conductive head-to-head dimeric form, but not in the double-helical dimeric form.

White *et al.* found for the conductivity of an aqueous layer between an sBLM and a glass support a value as small as 0.0026 $\Omega^{-1}cm^{-1}$.[34] The access resistance of a hypothetic conductive channel in an sBLM would be increased severely due to the proximity of the support to the channel mouth. Based on these facts, we assume that all conductive dimers that are electrically accessible and contribute to the measured conductance are located in the pore-spanning region of the bilayer. We further assume (1) 250 $Å^2$ per gramicidin monomer as well as conductive dimer,[54] (2) unitary conductance of 10 pS of a gD channel in a DPhPC bilayer in 100 mM KCl,[55] and (3) 76 $Å^2$ per DPhPC molecule.[56] The minimum measured resistance of 34 MΩ then corresponds to ~3000 gD channels open simultaneously in the membrane, which translates to a molar gD-to-lipid ratio of 1 : 24. The highest available value of the dimerization constant for gD in PC bilayers is $\sim 5 \times 10^{-14}$ mol cm^{-2}.[57] $K = [M]^2/[D]$, where $[M]$ and $[D]$ are the monomer and dimer surface densities, respectively. In our case, $[D]$ is $\sim 8.5 \times 10^{-12}$ mol cm^{-2}, hence $[M] \approx 6.5 \times 10^{-13}$ mol cm^{-2} per bilayer and 3.3×10^{-13} mol cm^{-2} monomers per monolayer leaflet. Only ~4% of the gD molecules are monomeric at this very high surface density, whereas the rest are agglomerated in conductive dimers. Please note that a smaller K would generate a proportion of free monomers even lower than 4%. The estimate of the molar gD-to-lipid ratio corrected for monomeric gD evaluates to ~1 : 23. The channel density attained here is considerably higher than that of $\sim 5 \times 10^{-14}$ mol cm^{-2}, which was identified previously as limiting for accurate conductance measurements in a standard painted BLM setup.[57] An electrical measurement at comparably high channel surface densities has not been reported before. Reduction of the bilayer area to below 0.1 μm^2 without the penalty of a high aperture

aspect ratio, as presented here, shifts the window of accessible channel densities toward considerably higher values. A possibility thus emerges of probing lipid–protein and protein–protein interactions at saturating protein densities directly by electrical means. Given the fact that the intra-membraneous perimeter of a gD monomer is expected to accommodate 7–8 diacyl lipids,[58] the calculated peptide–lipid ratio suggests that a peptide density has been reached where such phenomena might be coming into play.

3.7 Single-channel recordings of alamethicin in npsBLMs

dc current recordings through single peptide channels inserted in npsBLMs were conducted with the fungal peptide antibiotic alamethicin (Alm), as an example. For this purpose, dielectric properties of the Si_3N_4 windows were improved by a polymerized organic coating (see section S1 of ESI†). It should be emphasized that this paper does not intend to provide new insights on Alm channels. The purpose is rather to demonstrate that quality single-channel recordings can be obtained in oligo-arrays of the npsBLMs described here.

Discrete current steps typical of transitions between individual conductance states of the transmembrane permeable bundle formed by Alm monomers were observed.[59–61] An example of a trace of ionic conductance of a single Alm channel in an npsBLM and a corresponding amplitude histogram are shown in Fig. 9. Five discrete levels of conductance are evident. Normal distributions fitted to the particular histogram peaks yield conductance levels of 174 ± 13 pS, 756 ± 18 pS, 1460 ± 16 pS, and 2040 ± 20 pS after subtraction of background conductance (G_0). Ohmic behavior of the respective conductance states was seen in the npsBLMs, in agreement with the previous studies of Alm channels using Muller–Rudin,[62–64] Montal–Mueller,[65–67] and other lipid bilayer systems.[25,68] Lifetimes of the individual substates were in the millisecond range, while a channel as a whole would remain assembled for seconds, as reported before.[60] The characteristic induction of channel assembly by transmembrane potential was observed, manifested as current bursts of longer duration and higher frequency, increased probability that higher conductance states of the channel are occupied, and simultaneous opening of multiple channels (results not shown).[59] Delivery of Alm into the npsBLMs *via* perfusion was possible from the top as well as the bottom compartment of the cell. No decrease of the rate of Alm insertion into the bilayers was observed *via* the bottom (*i.e.* through the pores) relative to the top, presumably due to the low aspect ratio of the pores. Even without particular optimization, the system exhibited acceptable noise performance (<2 pA rms for a 500 MΩ feedback resistor and a 3 kHz Bessel filter cutoff), showing that the npsBLMs are suitable for single-channel recordings.

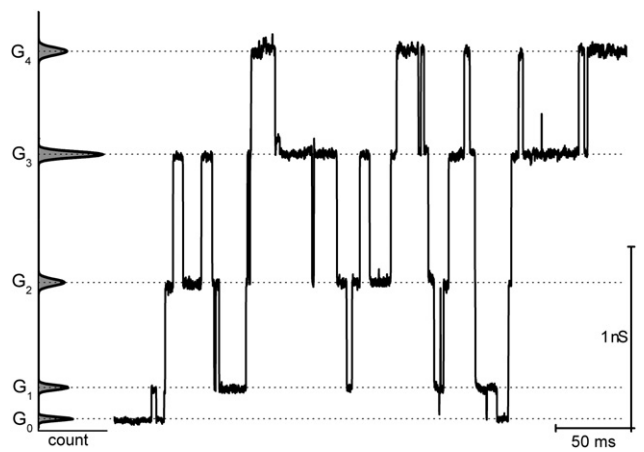

Fig. 9 An example of a *G vs.* time trace (right) and a corresponding histogram (left) of a single alamethicin (Alm) channel in an npsBLM. The trace was acquired at 130 mV dc (positive on the Alm side) in 0.95 M KCl, 5mM HEPES, pH 7. Alm was introduced into the npsBLMs from the pit side of the Si_3N_4 diaphragm through the pores by perfusion of the bottom compartment with the base electrolyte containing 500 nM Alm. The vertical axes of the histogram and the *G vs.* time trace are aligned and scaled equally. The data are presented as recorded (analog 4-pole Bessel filter, 3 kHz cutoff).

Conclusion

Formation of *solvent-free* npsBLMs over *arrays* of through nanopores has been accomplished by *directed* fusion of GUVs. Mechanical maneuvering of GUVs before fusion was instrumental to reliably span all pores of an array with npsBLMs. We have shown that the pores milled through Si_3N_4 diaphragms by an FIB are very well defined and allow for npsBLMs of high stability and electrical resistance. Minimum breakdown voltages of 250 mV of individual npsBLMs in an array are well in the range compatible with electrophysiological experiments. The possibility of probing protein–lipid interactions electrically *via* npsBLMs has been indicated by measurements of ionic currents through gramicidin channels at unprecedented peptide-to-lipid ratios. Modification of porous substrates by an organic coating has been shown to provide for chip dielectric properties consistent with protein single-channel recordings. Hospitality of the platform to transmembrane protein is further enhanced by full structural continuity of the fluidic phospholipid bilayer between the pore-spanning and the supported regions. Thereby, it should be possible for the assembled protein to diffuse between the two without loss of functional folding. The design of the platform allows for facile bilateral chemical, electrical, and optical access to the bilayers. We thus expect the npsBLMs presented here to make an impact on membrane protein research and inspire the design of functional assays for membrane protein drug targets.

Doubts may perhaps emerge with respect to the apparent discrepancy between the somewhat sophisticated technology (FIB, SEM, AFM) required to accomplish the results presented here and the prospected wide applicability of the platform to membrane protein research and pharmacology. It must be emphasized therefore that the platform is currently in a prototype phase. A plethora of unknowns still exist with respect to vesicle-derived npsBLMs over arrays of nanopores. For example, the impact of pore array parameters (*e.g.* pore size, topography, quantity per array, pore-to-pore distance, *etc.*), surface functionalization (hydrophilic/hydrophobic), or lipid composition (surface charge, fluidity, intrinsic curvature), to name a few, on the stability and properties of the npsBLMs must be understood. The FIB, which might be argued against as expensive and slow, is the only instrument capable of generating nanoscopic pores through Si_3N_4 diaphragms at the required

precision at present. Similarly, there is hardly a substitute for SEM and AFM in terms of the informative detail on the nanostructures these techniques deliver, detail, without which the above relationships cannot be determined. Cheaper and faster approaches, such as e-beam or colloidal lithography,[69] can be employed to fabricate nanoporous Si_3N_4 diaphragms at large scale once the optimum array parameters had been identified. After a reproducible process of pore fabrication at wafer level has been established, nanoscopic inspection of the features on every diaphragm will not be required any more. This work has provided a guideline to reach that stage. We believe that the approach presented here can provide a deeper insight into the biophysics of npsBLMs, and that this understanding will pave the way toward npsBLMs forming spontaneously from submicrometre (proteo)lipid vesicles and sealing multitudes of pores perfectly, as craved for by many a drug designer or electrophysiologist.

Acknowledgements

This work was financially supported by the EU through projects MEST-CT-2004-513924 and FM7 ASMENA-214666, and by the Slovak Scientific Grant Agency through the VEGA 1/4016/07 grant. The expertise of Dr Michael Kappl and Maren Mueller regarding the FIB is gratefully acknowledged.

References

1 W. F. Wonderlin, A. Finkel and R. J. French, *Biophys. J.*, 1990, **58**, 289–297.
2 M. Mayer, J. K. Kriebel, M. T. Tosteson and G. M. Whitesides, *Biophys. J.*, 2003, **85**, 2684–2695.
3 H. Suzuki, K. V. Tabata, H. Noji and S. Takeuchi, *Langmuir*, 2006, **22**, 1937–1942.
4 K. G. Klemic, J. F. Klemic, M. A. Reed and F. J. Sigworth, *Biosens. Bioelectron.*, 2002, **17**, 597–604.
5 N. Fertig, C. Meyer, R. H. Blick, C. Trautmann and J. C. Behrends, *Phys. Rev. E: Stat. Phys., Plasmas, Fluids, Relat. Interdiscip. Top.*, 2001, **64**, 040901–040904.
6 N. Fertig, R. H. Blick and J. C. Behrends, *Biophys. J.*, 2002, **82**, 3056–3062.
7 R. Pantoja, J. M. Nagarah, D. M. Starace, N. A. Melosh, R. Blunck, F. Bezanilla and J. R. Heath, *Biosens. Bioelectron.*, 2004, **20**, 509–517.
8 W. Romer, Y. H. Lam, D. Fischer, A. Watts, W. B. Fischer, P. Goring, R. B. Wehrspohn, U. Gosele and C. Steinem, *J. Am. Chem. Soc.*, 2004, **126**, 16267–16274.
9 D. Weiskopf, E. K. Schmitt, M. H. Kluhr, S. K. Dertinger and C. Steinem, *Langmuir*, 2007, **23**, 9134–9139.
10 W. Romer and C. Steinem, *Biophys. J.*, 2004, **86**, 955–965.
11 E. K. Schmitt, M. Vrouenraets and C. Steinem, *Biophys. J.*, 2006, **91**, 2163–2171.
12 X. J. Han, A. Studer, H. Sehr, I. Geissbuhler, M. Di Berardino, F. K. Winkler and L. X. Tiefenauer, *Adv. Mater.*, 2007, **19**, 4466–4470.
13 G. Baaken, M. Sondermann, C. Schlemmer, J. Ruhe and J. C. Behrends, *Lab Chip*, 2008, **8**, 938–944.
14 P. Mueller and D. O. Rudin, *Nature*, 1968, **217**, 713–719.
15 D. J. Woodbury and C. Miller, *Biophys. J.*, 1990, **58**, 833–839.
16 A. A. Seddon, P. Curnow and P. J. Booth, *Biochim. Biophys. Acta, Biomembr.*, 2004, **1666**, 105–117.
17 C. Hennesthal, J. Drexler and C. Steinem, *ChemPhysChem*, 2002, **3**, 885–889.
18 J. Drexler and C. Steinem, *J. Phys. Chem. B*, 2003, **107**, 11245–11254.
19 S. Steltenkamp, M. M. Muller, M. Deserno, C. Hennesthal, C. Steinem and A. Janshoff, *Biophys. J.*, 2006, **91**, 217–226.
20 O. Worsfold, N. H. Voelcker and T. Nishiya, *Langmuir*, 2006, **22**, 7078–7083.
21 N. Fertig, A. Tilke, R. H. Blick, J. P. Kotthaus, J. C. Behrends and G. ten Bruggencate, *Appl. Phys. Lett.*, 2000, **77**, 1218–1220.
22 A. P. Quist, A. Chand, S. Ramachandran, C. Daraio, S. Jin and R. Lal, *Langmuir*, 2007, **23**, 1375–1380.
23 C. Danelon, J. B. Perez, C. Santschi, J. Brugger and H. Vogel, *Langmuir*, 2006, **22**, 22–25.
24 C. Schmidt, M. Mayer and H. Vogel, *Angew. Chem., Int. Ed.*, 2000, **39**, 3137–3140.
25 M. Sondermann, M. George, N. Fertig and J. C. Behrends, *Biochim. Biophys. Acta, Biomembr.*, 2006, **1758**, 545–551.
26 E. K. Schmitt, M. Nurnabi, R. J. Bushby and C. Steinem, *Soft Matter*, 2008, **4**, 250–253.
27 J. Vancea, G. Reiss, F. Schneider, K. Bauer and H. Hoffmann, *Surf. Sci.*, 1989, **218**, 108–126.
28 L. A. Giannuzzi, B. I. Prenitzer and B. W. Kempshall, in *Introduction to Focused Ion Beams: Instrumentation, Theory, Techniques and Practice*, Springer, New York, 2005, pp. 13–52.
29 C. A. Volkert and A. M. Minor, *MRS Bull.*, 2007, **32**, 389–395.
30 R. J. White, E. N. Ervin, T. Yang, X. Chen, S. Daniel, P. S. Cremer and H. S. White, *J. Am. Chem. Soc.*, 2007, **129**, 11766–11775.
31 N. Fertig, M. Klau, M. George, R. H. Blick and J. C. Behrends, *Appl. Phys. Lett.*, 2002, **81**, 4865–4867.
32 N. C. Li, S. F. Yu, C. C. Harrell and C. R. Martin, *Anal. Chem.*, 2004, **76**, 2025–2030.
33 E. N. Ervin, H. S. White, L. A. Baker and C. R. Martin, *Anal. Chem.*, 2006, **78**, 6535–6541.
34 R. J. White, B. Zhang, S. Daniel, J. M. Tang, E. N. Ervin, P. S. Cremer and H. S. White, *Langmuir*, 2006, **22**, 10777–10783.
35 P. Scopece, L. A. Baker, P. Ugo and C. R. Martin, *Nanotechnology*, 2006, **17**, 3951–3956.
36 W. Desorbo, *Nucl. Tracks Radiat. Meas.*, 1979, **3**, 13–32.
37 K. W. Pratt, W. F. Koch, Y. C. Wu and P. A. Berezansky, *Pure Appl. Chem.*, 2001, **73**, 1783–1793.
38 R. A. Horne and R. P. Young, *J. Phys. Chem.*, 1968, **72**, 1763–1767.
39 R. P. Richter, R. Berat and A. R. Brisson, *Langmuir*, 2006, **22**, 3497–3505.
40 A. L. Bernard, M. A. Guedeau-Boudeville, L. Jullien and J. M. di Meglio, *Langmuir*, 2000, **16**, 6809–6820.
41 A. L. Bernard, M. A. Guedeau-Boudeville, O. Sandre, S. Palacin, J. M. di Meglio and L. Jullien, *Langmuir*, 2000, **16**, 6801–6808.
42 C. Hamai, P. S. Cremer and S. M. Musser, *Biophys. J.*, 2007, **92**, 1988–1999.
43 A. Priel, Z. Gil, V. T. Moy, K. L. Magleby and S. D. Silberberg, *Biophys. J.*, 2007, **92**, 3893–3900.
44 J. Lin, M. Merzlyakov, K. Hristova and P. C. Searson, *Biointerphases*, 2008, **3**, FA33–FA40.
45 M. Chemla, V. Bertagna, R. Erre, F. Rouelle, S. Petitdidier and D. Levy, *Appl. Surf. Sci.*, 2004, **227**, 193–204.
46 J. C. Weaver and Y. A. Chizmadzhev, *Bioelectrochem. Bioenerg.*, 1996, **41**, 135–160.
47 M. Montal and P. Mueller, *Proc. Natl. Acad. Sci. U. S. A.*, 1972, **69**, 3561–3566.
48 I. Mey, M. Stephan, E. K. Schmitt, M. M. Müller, M. Ben Amar, C. Steinem and A. Janshoff, *J. Am. Chem. Soc.*, 2009, **131**, 7031–7039.
49 D. A. Kelkar and A. Chattopadhyay, *Biochim. Biophys. Acta, Biomembr.*, 2007, **1768**, 2011–2025.
50 V. B. Myers and D. A. Haydon, *Biochim. Biophys. Acta*, 1972, **274**, 313–322.
51 A. M. O'Connell, R. E. Koeppe and O. S. Andersen, *Science*, 1990, **250**, 1256–1259.
52 J. A. Killian, *Biochim. Biophys. Acta*, 1992, **1113**, 391–425.
53 R. K. Chitta and M. L. Gross, *Biophys. J.*, 2004, **86**, 473–479.
54 R. R. Ketchem, B. Roux and T. A. Cross, *Structure*, 1997, **5**, 1655–1669.
55 A. Schatz, A. LinkeHommes and J. Neubert, *Eur. Biophys. J. Biophys. Lett.*, 1996, **25**, 37–41.
56 Y. L. Wu, K. He, S. J. Ludtke and H. W. Huang, *Biophys. J.*, 1995, **68**, 2361–2369.
57 W. R. Veatch, R. Mathies, M. Eisenberg and L. Stryer, *J. Mol. Biol.*, 1975, **99**, 75–92.
58 Z. Kota, T. Pali and D. Marsh, *Biophys. J.*, 2004, **86**, 1521–1531.
59 R. Latorre and O. Alvarez, *Physiol. Rev.*, 1981, **61**, 77–150.
60 G. A. Woolley and B. A. Wallace, *J. Membr. Biol.*, 1992, **129**, 109–136.
61 H. Duclohier and H. Wroblewski, *J. Membr. Biol.*, 2001, **184**, 1–12.

62 M. Eisenberg, J. E. Hall and C. A. Mead, *J. Membr. Biol.*, 1973, **14**, 143–176.
63 G. Boheim, *J. Membr. Biol.*, 1974, **19**, 277–303.
64 L. G. M. Gordon and D. A. Haydon, *Biochim. Biophys. Acta*, 1976, **436**, 541–556.
65 J. J. Donovan and R. Latorre, *J. Gen. Physiol.*, 1979, **73**, 425–451.
66 S. M. Bezrukov and I. Vodyanoy, *Biophys. J.*, 1993, **64**, 16–25.
67 I. Vodyanoy, S. M. Bezrukov and V. A. Parsegian, *Biophys. J.*, 1993, **65**, 2097–2105.
68 D. O. D. Mak and W. W. Webb, *Biophys. J.*, 1995, **69**, 2323–2336.
69 E. Reimhult, K. Kumar and W. Knoll, *Nanotechnology*, 2007, **18**, 275303.

